MERCK

catch the sun

Product Category list:

- Organic Photovoltaic (OPV) Donors and Acceptors
- Dye-Sensitized Solar Cell Materials
- Perovskite Materials

Visit us at:
SigmaAldrich.com/organic-electronics

MK_AD9792EN 43729 08/2022

The Life Science business of Merck operates as MilliporeSigma in the U.S. and Canada.

Sigma-Aldrich®
Lab & Production Materials

(040)-Crystal Facet Engineering of $BiVO_4$ Plate Photoanodes for Solar Fuel Production

*Chang Woo Kim, Young Seok Son, Myung Jong Kang, Do Yoon Kim, and Young Soo Kang**

A (040)-crystal facet engineered $BiVO_4$ ((040)-BVO) photoanode is investigated for solar fuel production. The (040)-BVO photoanode is favorable for improved charge carrier mobility and high photocatalytic active sites for solar light energy conversion. This crystal facet design of the (040)-BVO photoanode leads to an increase in the energy conversion efficiency for solar fuel production and an enhancement of the oxygen evolution rate. The photocurrent density of the (040)-BVO photoanode is determined to be 0.94 mA cm^{-2} under AM 1.5 G illumination and produces 42.1% of the absorbed photon-to-current conversion efficiency at 1.23 V (vs RHE, reversible hydrogen electrode). The enhanced charge separation efficiency and improved charge injection efficiency driven by (040) facet can produce hydrogen with 0.02 mmol h^{-1} at 1.23 V. The correlation between the (040)-BVO photoanode and the solar fuel production is investigated. The results provide a promising approach for the development of solar fuel production using a $BiVO_4$ photoanode.

1. Introduction

Photoelectrochemical (PEC) products in solar light water splitting have attracted much attention as an artificial photosynthesis.[1–5] Since the first demonstration by Fujishima and Honda,[6] recent developments and advances have been focused on PEC performance, which is considered to be the key challenge in developing a photoelectrode for the solar light water splitting reaction.[7–10] Theoretically, the efficient light absorption and favorable valence band edge of bismuth vanadate ($BiVO_4$) thin film allow for a maximum photocurrent density of 7.5 mA cm^{-2} under Air Mass 1.5 Global (AM 1.5 G) solar illumination.[4] Therefore, $BiVO_4$ has been proposed as the best PEC performance photocatalyst for solar light driven water oxidation reactions.[10–14] However, the practical photogenerated current of this photocatalyst is much lower than the theoretical calculation because of its inherent drawbacks, such as sluggish charge mobility and fast charge recombination, which result in limitations during practical application. Because the solar light conversion efficiency (η)[15] is directly proportional to the product of the solar light absorption efficiency (η_{abs}), charge separation efficiency (η_{sep}), and surface charge transfer efficiency (η_{trans}). The decoration of the cocatalyst[16] and the introduction of porosity to increase surface area[17] have been studied for practical usage of PEC with increased η_{abs}, η_{sep}, and η_{trans}. Specifically, recent developments in the fully integrated nanowire-based heterostructure[18,19] and the introduction of a dual-layer oxidation cocatalyst[20] into porous $BiVO_4$ have been reported for practical solar fuel production with good η_{abs}, η_{sep}, and η_{tran}.

However, the typical PEC performance of a pristine $BiVO_4$ photoanode to produce solar fuel products is not impressive because it suffers from inherent drawbacks. The development and design of $BiVO_4$ microcrystals have been highlighted to produce solar fuel products by introducing photocatalytic crystal facet engineering and cocatalyst,[20–22] and the breakthrough for enhancing solar light conversion efficiency has not been suggested previously for a pristine $BiVO_4$ photoanode.

Here, a (040)-crystal facet engineered $BiVO_4$ ((040)-BVO) plate photoanode has been investigated to produce solar fuel products as an artificial photosynthesis with highly enhanced PEC performance via a crystal facet engineering approach that is based on reports by Cheng and co-workers[23,24] and Li and co-workers.[11,21,22] We demonstrate the higher PEC performance caused by higher efficient η_{sep} and η_{tran} of the BVO thin film with selectively exposed (040) crystal facet. Because the (040) facet-manipulated $BiVO_4$ plate photoanode has not been previously studied, our designed model demonstrates the significance of the interfacial electron transport reaction between the {010} plane and the electrolyte with η_{sep} and η_{tran}, resulting in the highest PEC performance. The results of this study may provide the most viable strategy for designing an efficient $BiVO_4$ photoanode for enhanced solar fuel production.

2. Results and Discussion

A (040)-crystal facet engineered $BiVO_4$ plate photoanode ((040)-BVO) was hydrothermally synthesized via a seed layer approach

Dr. C. W. Kim, Y. S. Son, M. J. Kang, D. Y. Kim, Prof. Y. S. Kang
Korea Center for Artificial Photosynthesis and Department of Chemistry
Sogang University
#1 Shinsu-dong, Mapo-gu, Seoul 121-742, South Korea
E-mail: yskang@sogang.ac.kr

DOI: 10.1002/aenm.201501754

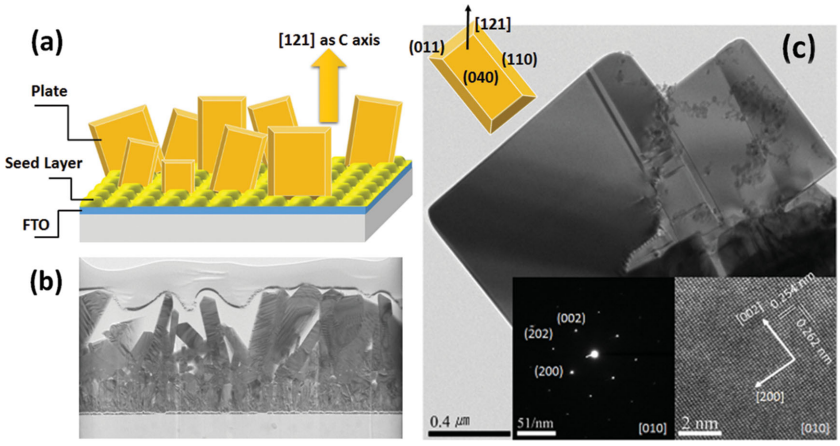

Figure 1. Scheme and transmission electron microscopy observation. Scheme of the a) (040)-crystal facet engineered $BiVO_4$ photoanode, b) focused ion beam-treated cross-sectional TEM image, and c) (040)-viewed HRTEM and SAED pattern of individual microplate. From the TEM images, the individual microplate with the lateral (040) facet in the photoanode was well grown on the seed layer.

by using a $TiCl_3$-structure directing agent (Ti-SDA). Microscopic observation provided information on the growth direction of (040)-BVO, as shown in **Figure 1**. High-resolution transmission electron microscopy (HRTEM) and selected-area electron diffraction (SAED) patterns viewed along the [010] direction showed that the plate shape $BiVO_4$ microcrystal grew vertically/hydrothermally along the [121] direction as dominant peak of XRD spectrum, corresponding to the c-axis from the $BiVO_4$ seed layer on the surface of fluorine doped tin oxide glass (FTO), resulting in the larger surface area of (040) crystal facet of $BiVO_4$ photoanode (Figure S1, Supporting Information). A well-defined $BiVO_4$ plate was observed as a single crystal plate with a length of approximately 1.5 μm and a thickness of approximately 650 nm. It is important to note that each individual $BiVO_4$ microcrystal appears to have a decahedral single crystal plate with 4-exposed (011) crystal facets and 4-exposed (110) crystal facets along with 2-exposed (010) crystal facets. In each individual plate of $BiVO_4$, 2-(010) crystal facets surrounding 4-(110) and 2-(011) crystal facets were grown with 2-(011) crystal facets hidden as a base for the seed layer. To better understand the crystal structure of the manipulated $BiVO_4$ microcrystal plate, the c-axis vertically growth direction from the $BiVO_4$ seed layer was matched along the [121] direction in the monoclinic structure, which was studied using X-ray powder diffraction (XRD) and a scanning electron microscopy (SEM) (**Figure 2**). Figure 2 shows SEM images of the top of the $BiVO_4$ seed layer (SL-BVO), $BiVO_4$ plate film (PF-BVO), and (040) facet-engineered $BiVO_4$ film ((040)-BVO), which depend on the amount of used Ti-SDA (Figure S2, Supporting Information). Interestingly, the exposed lateral side of individual plate became larger as the concentration of Ti-SDA increased but is free from Ti/Cl ion in Ti-SDA (Figures S3–S5, Supporting Information).[11] Thus, the affinity between SDA and the particular facet results in a specific microcrystal morphology by suppressing the growth of individual crystal facets.[24–26] All of the diffractions in the XRD pattern were well indexed to monoclinic scheelite $BiVO_4$ (JCPDS card #140688, space group: $I2/a$).[11] Because the (040) plane of the $BiVO_4$ microcrystal plate is positioned with the lateral side of each individual plate, the 2θ peak position

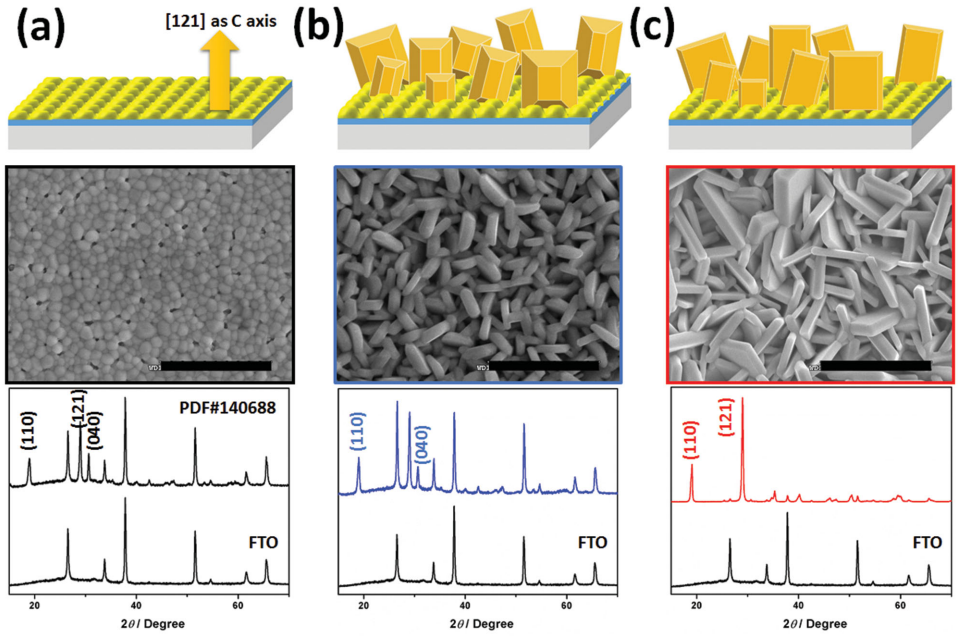

Figure 2. Morphological observation. Scheme of the a) top-viewed FESEM images and XRD pattern of the $BiVO_4$ seed layer, b) $BiVO_4$ plate film and c) (040) facet engineered $BiVO_4$ film. Exposed area of the lateral (040) facet depends on the use of a $TiCl_3$ solution. $BiVO_4$ plate film ((b), 0.06 mL of $TiCl_3$) and (040) facet engineered $BiVO_4$ film ((c), 0.12 mL of $TiCl_3$). Scale bar represents 5 μm.

of the (040) plane in the XRD pattern was located at 30.8° in SL-BVO and PF-BVO. It is important to note that the 2θ value of the lateral side is indistinct in (040)-BVO, which indicates that the peak position of the (040) facet in $BiVO_4$ is related to the exposure of the lateral side facet, as shown in the SEM images of Figure 2. Based on the seed layer approach, our microscopic and crystallographic observations support the vertical growth of the monoclinic scheelite (040)-BVO as a single-crystalline $BiVO_4$ microcrystal plate from a $BiVO_4$ seed layer on the FTO substrate.

As expected from the relationship between the exposed (040) facet and the PEC performance, the photoelectrochemical characteristics shown in **Figure 3** indicate that (040)-BVO produced the highest photocurrent density of 0.94 mA cm^{-2}, which was much larger than that of PF-BVO (0.35 mA cm^{-2}) and SL-BVO (0.1 mA cm^{-2}) at 1.23 V (vs RHE, reversible hydrogen electrode) under AM 1.5 G illumination. From each photocurrent response behavior, the photoelectrochemical significance can be determined. First, considering that current–voltage (*I–V*) behavior of SL-BVO have been clearly observed as that of a typical $BiVO_4$ photoanode, the comparative data is presented in Table S1 (Supporting Information). The exponential shape of photocurrent curve corresponds to the classical behavior of SL-BVO.[27]

It indicates that the photovoltaic performance in typical $BiVO_4$ inherently suffers from slower charge mobility and less charge separation, which resulted in a photocurrent density of 0.1 mA cm^{-2}.[17] Interestingly, as the (040)-crystal facet becomes exposed in PF-BVO, their *I–V* curve exhibits a straight line with slope, and the photocurrent density rapidly increased to 0.35 mA cm^{-2}. By considering that the photocurrent density reaches to 0.94 mA cm^{-2} with (040)-BVO, it is important to note that the (040) crystal facet drives the photogenerated charge flow and enhances charge separation and charge transfer. In addition, because the lower fill factor of the *I–V* curve represents the higher charge carrier recombination, the (040) crystal facet reduces charge trap sites for favorable charge transfer. Finally, for the water oxidation kinetics, SL-BVO exhibited an onset potential (V_{op}) of 0.66 V (vs RHE), which is typically observed in bulk $BiVO_4$ (Figure S6, Supporting Information).[28] The obtained transient photocurrent responses in the chopped light *I–V* curve of (040)-BVO indicate electron–hole recombination at the electrode/electrolyte interface.[29] Initially holes are accumulated at the solid/liquid interface because of slower kinetics of water oxidation. Therefore, it is end up with electron–hole recombination and generate initial spike in transient photocurrent. Finally steady-state photocurrent are observed, because smooth hole transfer takes place without electron–hole recombination. This process have been practically shown in transient photocurrent responses in the chopped light (Figure 3a). Interestingly, 0.43 V of V_{op} observed as cathodic shift in the photocurrent curve of PF-BVO. In addition, in the photocurrent curve, V_{op} exhibited a cathodic shift to 0.39 V for (040)-BVO. Because overpotential is required for the water oxidation reaction, in which the photogenerated charges accumulate and recombine at the semiconductor/liquid junction, the (040) crystal facet has a lower water oxidation energy barrier for interfacial charge transfer. PEC performance with H_2O_2 as a hole-scavenger has been confirmed to be enhanced as a lateral (040) crystal facet of $BiVO_4$ photoanode to be exposed as larger surface area in Figure S7 (Supporting Information).

Photocurrent density obtained from H_2O_2 oxidation reaction is following Equation[20,30]

$$J^{H_2O_2} = J_{abs} \times P_{char} \times P_{inj}$$

where, J_{abs} is the photon absorption rate, P_{char} is charge separation rate, and P_{inj} is charge injection rate.

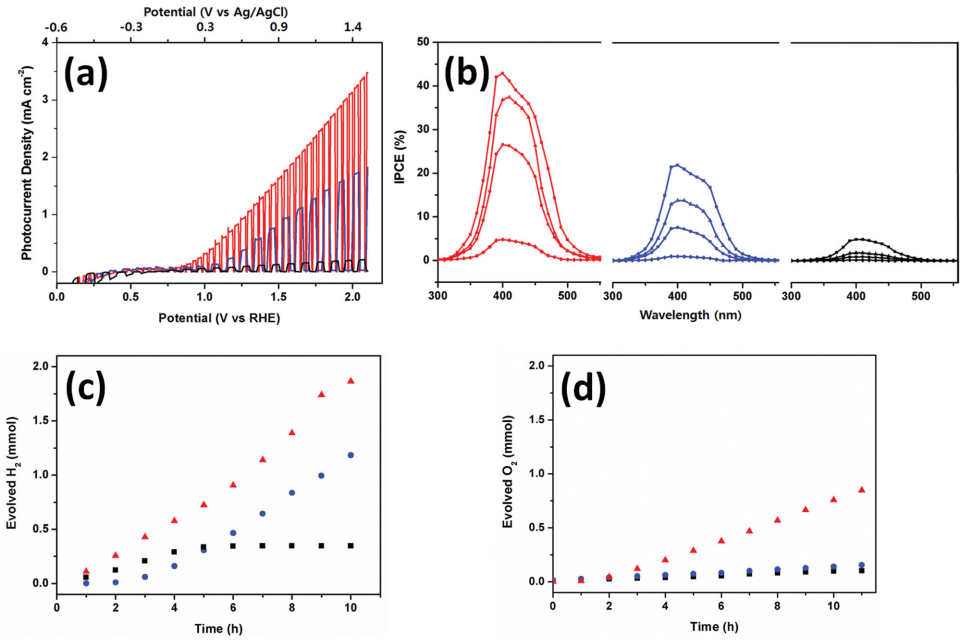

Figure 3. PEC characteristics and H_2/O_2 evolution measurement as a function of bias. a) *I–V* curves, b) IPCE, c) H_2 evolution measurement, and d) O_2 evolution measurement of the $BiVO_4$ seed layer (black), $BiVO_4$ plate film (blue), and (040) facet engineered $BiVO_4$ film (red). IPCE obtained at O V (◆), 0.3 V (●), 0.6 V (▲), and 1.0 V (■) versus Ag/AgCl. Gas evolution measured at 0.6 V (vs Ag/AgCl).

Considering fast oxidation kinetics in H_2O_2 electrolyte, it is clear that electron–hole recombination is negligible ($P_{inj} \approx 1$) at solid/liquid junction. In H_2O electrolyte, P_{inj} is calculated by taking ratio of J^{H_2O} and $J^{H_2O_2}$, which is equal to ≈39.5% at 1.23 V (vs RHE) as shown in Figure S7 (Supporting Information). The J_{abs} (3.158 mA cm^{-2}) of in (040)-BVO was calculated from absorption spectrum and P_{char} of (040)-BVO reached to 0.72 at 1.23 V (vs RHE). It is worthy note that P_{char} and P_{inj} increases dramatically as (040) facet get exposure. Even more, 0.72 of P_{char} is much more remarkable value with a best of our knowledge considering that a typical P_{char} for a pristine $BiVO_4$ photoanode is from 0.2 to 0.3 at 1.23 (vs RHE).[20,30]

These PEC characteristics, which depend on the (040)-crystal facet, were also observed in the incident photon to current conversion efficiency (IPCE). The onset photocurrent wavelength (λ_{op}) at 1.23 V (vs RHE) was 500 nm in SL-BVO, which is representative of typical bulk $BiVO_4$, as shown in Figure 3b and Figure S8 (Supporting Information). Notably, λ_{op} is shifted from 500 nm to 540 nm as the (040) crystal facet becomes exposed in PF-BVO and (040)-BVO. From the calculation of the absorbance in (040)-BVO, the solar light harvesting efficiency (LHE) reached 89% at between 375m and 480 nm, as shown in LHE of Figure S9 (Supporting Information) and optical absorbance of Figure S10 (Supporting Information). In particular, based on the observation of λ_{max} at 410 nm for (040)-BVO, its *I–V* curve exhibited a distinct behavior when (040)-BVO is exposed to 410 nm. The V_{op} (vs RHE) in (040)-BVO (i.e., 0.39 V) is very early among pristine $BiVO_4$ photoanode, and its photocurrent density rapidly increased from the potential at 0.6 V, which indicated the remarkable difference compared with SL-BVO. IPCE of (040)-BVO reaches 37.5%, which is the highest value compared to 1.8% and 13.9% for SL-BVO and in PF-BVO, respectively, at a bias potential of 1.23 V (vs RHE). The absorbed photon-to-current conversion efficiency (APCE) was 42.1% in (040)-BVO. Based on IPCE (%) = charge separation efficiency (η_{sep}) × charge transport efficiency (η_{trans}) × interfacial charge transfer efficiency (η_{inter}) at the interfacial solid–liquid junction, these IPCE and APCE characteristics are consistent with the fact that the (040) crystal facet leads to the higher solar light absorption and charge separation efficiency, considering that η_{inter} is considered with usage of cocatalyst.[15,19,31] The applied bias photon-to-current efficiency (ABPE) of (040)-BVO is calculated and plotted from its *I–V* curve in Figures S11 and S12 (Supporting Information), where 0.07% was obtained as a maximum ABPE at 1.05 V. Based on the enhanced η_{sep} and η_{trans} due to the exposed (040) crystal facet, the determined amount of O_2 and H_2 solar fuels was observed at 1.23 V (vs RHE) under AM 1.5 G illumination. In Figure 3c,d, the evolution of solar fuel products with (040)-BVO was impressive with respect to their accumulated amount of solar fuel and the long-term stability of the photoanode. The hydrogen evolution rate in (040)-BVO was about 0.02 mmol h^{-1} compared with 0.007 mmol h^{-1} and 0.002 mmol h^{-1} using PF-BVO and SL-BVO, respectively. For O_2 evolution, 0.01 mmol h^{-1} was produced in (040)-BVO, which was very high. In addition to the PEC characteristics, favorable water oxidation rate was achieved with enhanced η_{inter} in (040)-BVO and resulted in 100% of faradaic efficiency of accumulated solar fuel products. (see calculation in the Supporting Information) The evolution reactions of the solar fuel products were stable over 40 h due to the long-term stability of the (040)-BVO photoanode (Figure S12, Supporting Information).

To date, PEC enhancement has been predicted and systematically demonstrated based on the relationship between the higher surface energy and the photocatalytic/PEC performance.[32,33] In this study, order of specific surface area did not show the reason why PEC performance was improved in (040)-BVO (Figure S13, Supporting Information). To understand the enhanced PEC performance in (040)-BVO, the surface energy of the typical facets of the $BiVO_4$ crystal was calculated and compared in Figure S14 and Table S2 (Supporting Information). For water molecule dissociation by the photogenerated charge, the active sites in the $BiVO_4$ crystal facet should include a Bi atom at the topmost layer with dangling bonds, which results in a high surface energy.[32,33] The (001) surface is terminated with only unsaturated oxygen atoms, and the (040) plane contains two unsaturated oxygen atoms and unsaturated metal atoms in the topmost layer. Therefore, the (001) facet has the largest surface energy of 2.5234 J m^{-2} compared with 1.6997 J m^{-2} for the (110) facet and 0.6119 J m^{-2} for the (011) facet. However, the surface energy was determined to be 0.0479 J m^{-2} in the (040) plane based on the number of dangling bonds from the exposed atom. Especially, in the semiconducting photocatalysts such as $BiVO_4$ and TiO_2, there is still significant controversy on the relationship between surface energy and photocatalytic/PEC performance in the literatures.[23,25] Due to the difference of the energy level between the conduction band (CB) and valence band (VB) of $BiVO_4$ calculated for {110} and {010}, photogenerated electron transport is thermodynamically favorable from CB(110) to CB(010) in $BiVO_4$.[22] Therefore, the geometric structure of the surface affects the adsorption and desorption behavior of water molecules.[34] The X-ray absorption near-edge structure (XANES) and extended X-ray absorption fine structures (EXAFS) were determined to identify the geometry of (040)-BVO during the PEC measurement. As shown in the EXAFS result of **Figure 4**, the neighboring oxygen is far from the Bi atom under illumination compared to the distance between oxygen and Bi atom. In the fluorescence mode, the Bi L_3-edge XANES spectra are similar with and without illumination (Figure S15, Supporting Information). In particular, the pre-edge peak corresponding to a 2p → 6s transition was not observed in either case, which indicated that the oxidation states of Bi^{3+} with a full $6s_2$ configuration in (040)-BVO remains constant during the PEC reaction. To clarify the local surface structure of the Bi L_3-edge in (040)-BVO, Fourier-transformed spectra of EXAFS were compared during the water oxidation reaction. Under dark conditions, two major peaks appear at 1.60 Å and 3.07 Å, which correspond to the Bi-O, and Bi-V distance, respectively. Interestingly, during the water oxidation reaction, these two major peaks are slightly shifted to 1.63 Å and to 3.10 Å, which is indicative of the increasing Bi-O and Bi-V distance, respectively. In addition, the Bi-O peak intensity was comparatively lower during the water oxidation reaction. These two kinds of change demonstrate that the structural ordering was disturbed and the Bi-O and Bi-V distances were simultaneously increased, especially on the surface.[12] In the water splitting reaction, charge separation by photon absorption occur and it accumulates at

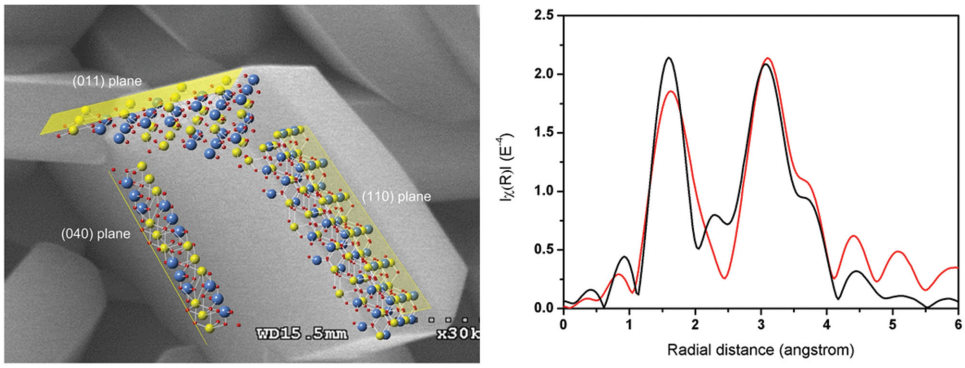

Figure 4. Geometrical structure and EXAFS. a) Geometrical structure (yellow, blue, red color, and yellowish area stand for Bi, V, O atom, and exposed plane respectively) and b) EXAFS of a single individual plate of the (040) facet engineered $BiVO_4$ film (dark condition; black, illumination, red). Bi-O and Bi-V distances were enhanced in the Bi L_3-edge EXAFS measured during the PEC reaction at 1.23 V (vs RHE).

the semiconductor/electrolyte interface. With the adsorption of water molecules on the exposed Bi atom on the (040)-BVO surface, the exposed Bi atom would be far from the internal oxygen atom during the solar irradiation. It weakens the backscattering signal of photo-electron in the absorber-neighbor (Bi-O) scattering events compared with the dark condition.[35] Because the photo-electron from the absorbing Bi atom could scatter from a neighboring O atom in XAFS, the scattered photo-electron modulates the amplitude of the photo-electron wave-function at the absorbing Bi atom.[36] It indicates that the Bi-O distance increase and atomic ordering on the topmost layer is disordered during water splitting reaction.

We assume that the charge transfer from the Bi atom to the adsorbed H_2O molecules is highly activated at (040) facet/water interface. Based on the concept of surface-bound species,[37] two active sites are required for two water molecule adsorption during the oxygen evolution process. For more efficient water splitting, the (040) facet provides more favorable local bonding geometry for water molecule adsorption. Based on our observations, the origin of the highly efficient solar fuel production on (040)-BVO was due to a synergistic effect between the enhanced charge mobility and local bonding geometry to get lower energy barrier for the efficient charge transfer through the interface. It is consistent with recent reports with facet depending conductivity[38] and interfacial charge diffusivity along *c*-axis to substrate.[39] Especially, based on that the Nyquist plots is attributed to the interfacial charge transfer kinetics, the recombination resistance at the interface between the surface of BVO thin film photoanode and electrolyte solution increases in the following order: (040)-BVO < PF-BVO < SL-BVO in Figure S16 (Supporting Information). Among them, (040)-BVO exhibits the highest photovoltaic performance, owing to its low interfacial impedance for charge transfer.

Table 1. Decay time on time-resolved photoluminescence (TRPL). Decay time of the charge carriers in the (040) facet engineered $BiVO_4$ film was enhanced.

Emission	$BiVO_4$ seed layer	$BiVO_4$ plate film	(040) facet engineered $BiVO_4$ film
406 nm	49.52 ns	57.99 ns	64.88 ns
550 nm	31.64 ns	58.28 ns	69.62 ns
600 nm	40.45 ns	59.03 ns	71.41 ns

To a significant extent, this enhanced PEC performance for the kinetics of photogenerated charge carriers was confirmed with time-resolved photoluminescence (TRPL) at room temperature. From the excitation wavelength at 375 nm, transient emission was observed at 406, 550, and 600 nm in SL-BVO (black), PF-BVO (blue), and (040)-BVO (red), respectively. As summarized in **Table 1** and **Figure 5**, the average decay time (τ_{ave}) of the charge carriers in (040)-BVO was 64.88, 69.62, and 71.41 ns at the emitted 406, 550, and 600 nm, respectively. Because the accumulation of photogenerated charges at the surface drives water oxidation kinetics for higher charge separation efficiency as shown in PEC performances using hole scavenger of Figure S7 (Supporting Information), τ_{ave} of the charge carriers in (040)-BVO is significantly increased compared with those in SL-BVO and PF-BVO, which indicates that the (040)-crystal facet enhances the charge separation efficiency and suppresses charge recombination at the interfacial solid–liquid junction.

3. Conclusions

In conclusion, the introduction of the (040) crystal facet into the $BiVO_4$ photoanode has several significant consequences for solar fuel production. First, the (040) crystal facet results in an accumulation of photogenerated charges and retards the charge recombination rate to enhance the charge separation efficiency and charge transport efficiency. A long-lived charge, which is accumulated at the interfacial junction, promotes the water oxidation kinetics obtained from the geometric structure of the (040) facet. Therefore, our results on the enhanced photoelectrochemical performance from the facet crystal engineering $BiVO_4$ photoanode can bring a much more improved PEC performance via surface modification with appropriate cocatalysts in addition to the introduction of dopants and morphology engineering. Based on this research, these results are expected to be applicable to other metal oxide photoelectrodes and have provided preliminary insight into the origin of the photoelectrochemical performance of the (040) crystal facet of the $BiVO_4$ photoanode.

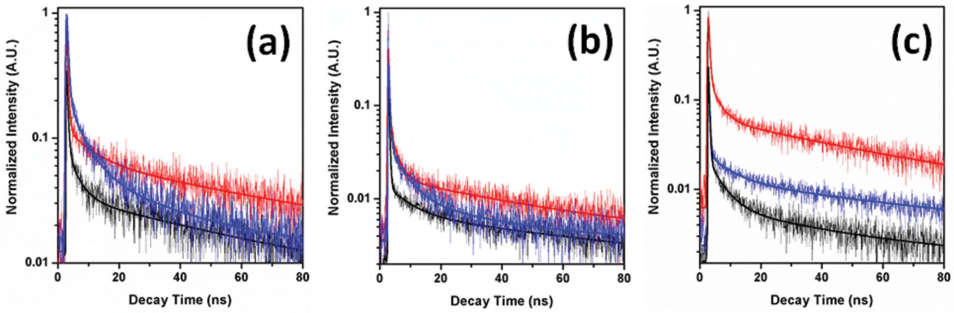

Figure 5. Time-resolved photoluminescence (TRPL). TRPL of the $BiVO_4$ seed layer (black), $BiVO_4$ plate film (blue), and (040) facet engineered $BiVO_4$ film (red). Transient emission observed at a) 406 nm, b) 550 nm, and c) 600 nm at an excitation of 375 nm at room temperature. Based on a comparison, the decay time of the charge carriers for the (040) facet engineered $BiVO_4$ film (red) was enhanced.

4. Experimental Section

Methods: The synthetic procedure for the (040)-crystal facet engineered $BiVO_4$ photoanode ((040)-BVO) was modified from that reported by Li and co-workers.[11] For the $BiVO_4$ seed layer on the FTO (TEC-8, 6–9 Ω sq^{-1}, 2.0 cm × 2.0 cm) substrate, $Bi(NO_3)_3{\cdot}5H_2O$ (5 mmol, 2.4254 g, Sigma-Aldrich 98%), NH_4VO_3 (5 mmol, 0.5849 g, Sigma-Aldrich), and citric acid (2-hydroxypropane-1,2,3-tricarboxylic acid, 10 mmol, Daejung, Monohydrate 99.5%) were dissolved in 15 mL of 23.3% HNO_3 aqueous solution (v/v of 60% HNO_3 and distilled water, 0.63/1) and stirred for 30 min. The transparent blue colored solution was placed into acetic acid (3.75 mL) with polyvinyl alcohol (PVA, 1.2 g, Aldrich, Mw 89 000–98 000, 99+% hydrolyzed) and stirred vigorously until the solution became transparent (i.e., approximately for 6 h). The solution was dropped and spin-coated on a clean FTO substrate at 1000 rpm for 20 s and followed by heat treatment at 723 K for 4 h in air. For a typical synthetic procedure to prepare (040)-BVO, $Bi(NO_3)_3{\cdot}5H_2O$ (4 mmol, 0.1164 g) and NH_4VO_3 (4 mmol, 0.028 g) were dissolved in 60 mL of a 2.0 M HNO_3 aqueous solution. 0.093 μmol of a titanium (III) chloride solution ($TiCl_3$ in 20–30 wt% HCl, Sigma-Aldrich, 0.12 mL) was added to the solution as a structure-directing agent (SDA). After the pH of the reaction solution was adjusted to 0.9 using an ammonia solution (NH_4OH, JIN Chemical, 25–28 wt%), the solution was transferred to a Teflon-lined autoclave (75 mL). The prefabricated $BiVO_4$ seed layer on the FTO substrate was immersed in the reaction solution and allowed to react at 180 °C for 12 h. The hydrothermally reacted substrate was heat treated at 773 K for 4 h. For manipulation of the exposed (040) facet area, the amount of $TiCl_3$ solution was varied from 0.24 to 0 mL. In particular, 0.6 mL of the $TiCl_3$ solution was used for PF-BVO, and 0.12 mL of the $TiCl_3$ solution was used for (040)-BVO.

Materials Characterization: The crystallographic information for the $BiVO_4$ photoanodes was obtained by X-ray diffraction (XRD, Rigaku miniFlex-II desktop X-ray diffractometer, Cu Kα radiation with λ = 0.154056 nm). The microscopic observation of the $BiVO_4$ photoanodes was carried out using SEM (Hitachi S-4300 FE-SEM) equipped with Oxford JEM-2010 energy dispersive spectroscopy (EDS). The TEM image and SAED pattern were obtained using a JEOL transmission electron microscope (JEM 2100F) at an accelerating voltage of 200 keV. The optical properties including the band gap of $BiVO_4$ were monitored and determined from diffuse reflectance spectroscopy (DRS) using a Varian Cary 5000 UV–vis–NIR Spectrophotometer (Agilent Technologies), and the FTO glass was used as the reference to characterize the absorbance.

Photoelectrochemical Measurements: The photoelectrochemical measurements of the $BiVO_4$ photoanodes as working electrodes in a conventional three-electrode system were performed using a PL-9 potentiostat. A 300 W Xe arc lamp was used for simulated solar illumination with an AM 1.5G filter (Asahi HAL-320, 100 mW cm^{-2}). Prior to the PEC measurement, the power density of the incident light was adjusted to 100 mW cm^{-2} using a NREL certified reference cell (Photo Emission Tech., Inc.). The illumination was set as a backside illumination to the FTO surface. The illuminated area was 0.636 cm^2 of a circle with a diameter of 0.9 cm in 4 cm^2 of the $BiVO_4$ photoanodes. Using a Pt electrode and Ag/AgCl reference electrode in an aqueous Na_2SO_4 solution (0.5 M, pH = 6.8), the *I–V* curves were plotted at a scan rate of 20 mV s^{-1} by sweeping the potential in the positive direction. The *I–t* curve was observed under constant bias. All of the PEC measurements were performed using a Ag/AgCl (2.0 M of KCl) reference electrode at room temperature, and then, the applied bias was converted to the reversible hydrogen electrode (RHE) using the following Nernst equation[15,20,31]

$$E_{RHE} = E_{Ag/AgCl} + E^{\circ}_{Ag/AgCl\ versus\ NHE} + 0.0591V \times pH$$
$$(E^{\circ}_{Ag/AgCl\ vs\ NHE} = 0.1976V\ vs\ NHE\ at\ 25\ ^{\circ}C)$$

where E_{RHE} is the potential versus RHE, 0.0 V versus RHE for water oxidation, E_{RHE} is the experimental potential measured versus the Ag/AgCl reference electrode, and $E^{\circ}_{Ag/AgCl\ versus\ NHE}$ is the standard potential of the Ag/AgCl versus NHE (0.1976 V at 25 °C). The incident photon to current conversion efficiency (IPCE) from 300 to 600 nm was determined with an applied potential of 0, 0.3, 0.6, and 1.0 V (vs Ag/AgCl). An Oriel Cornerstone 130 monochromator was used to produce monochromatic light with an interval of 10 nm. The light harvesting efficiency (LHE) at each wavelength was calculated from the absorbance using the following equation[15,20,31]

$$LHE = 1 - 10^{-A(\lambda)}\ (A(\lambda)\text{: absorbance at wave length } \lambda)$$

Based on LHE and IPCE, the absorbed photon-to-current efficiency (APCE) was determined at each wavelength using the following equation[15,20,31]

$$APCE(\%) = IPCE(\%)/LHE$$

From the *I–V* curve, the applied bias photon-to-current efficiency (ABPE) was calculated using the following equation[15,20,31]

$$ABPE\ (\%) \frac{J\left(\frac{mA}{cm^2}\right) \times (1.23 - V_{bias})(V)}{P_{in}\left(\frac{mW}{cm^2}\right)} \times 100\%$$

P_{char} and P_{inj} were calculated by the rate of J^{H_2O} and $J^{H_2O_2}$. The 0.5 M of H_2O_2 (Daejung Chemicals) was added into 0.5 M Na_2SO_4 electrolyte.[30]

Solar Light Fuel Production Measurements: The hydrogen and oxygen evolution experiments were carried out in an airtight continuous flow cell connected to an online GC system (Agilent 7890A) equipped with a pulsed discharged detector (PDD). A 30 mL PEC cell consisted of Nafion

117 proton transfer material between the $BiVO_4$ photoanode and Pt counter electrode. 1.13 cm^2 of illuminated area in the $BiVO_4$ photoanode and the Pt counter electrode was separately applied to 15 mL of 0.5 M Na_2SO_4 aqueous solution with Ag/AgCl as a reference electrode. After He gas (99.9999%) was used at a flow rate 6 mL min^{-1} for 3 h to remove the air under dark conditions, the working electrode was illuminated under a continuous flow of He (6 mL min^{-1}). The evolved gas was evaluated every hour for 12 h reaction at 0.6 V (vs Ag/AgCl).

Simultaneous X-Ray Absorption Analysis with PEC Analysis: X-ray absorption analysis of the $BiVO_4$ photoanodes was carried out with the PEC measurement. The PEC cell was set according to the previously mentioned conditions. The local bonding structure of $BiVO_4$ in a 0.5 M Na_2SO_4 (pH 6.8) electrolyte with a potentiostat (Ivium compactstat) was measured using X-ray Absorption Fine Structure (XAFS) with a synchrotron radiation beam at the Pohang Accelerator Laboratory (PAL) 10C beam line. Both dark conditions without external potential and 1 sun light illumination with 600 mV external potential versus Ag/AgCl reference electrode were employed. The measured XAFS data have been refined into X-ray absorption near edge spectra (XANES) and extended X-ray absorption fine structure (EXAFS), and fitted by computational calculations using the IFEFFIT algorithm.

Computational Calculation: The surface energy (γ) was obtained using the following equation: $\gamma = \left(E_{slab} - \frac{N}{n}E_{bulk}\right)/2A$, where E_{slab} is the total energy of the material that contains a surface in particular direction, E_{bulk} is for the total energy of the bulk structure, N is the total number of atoms in a unit cell, n is the total number of atoms in the bulk unit cell, and A is the area of the surface of the material. Schematic illustrations of the unit cell structures of the bulk and five different surface geometries, such as $BiVO_4$ (004), $BiVO_4$ (110), $BiVO_4$ (011), $BiVO_4$ (121), and $BiVO_4$ (010) systems, have been provided. It is important to note that the red, blue, and gray balls represent O, Bi, and V atoms, respectively. After cleaving the bulk material in each surface direction, the unit cell contained 72 atoms, and the bulk $BiVO_4$ contained 24 atoms in the monoclinic unit cell. Each system has an oxygen-terminated surface, and the stoichiometric ratio was maintained. Because the $BiVO_4$ has a monoclinic structure in the bulk, each system has different lattice parameters after cleaving from the bulk. The total energy calculation was performed using the Vienna ab initio simulation package (VASP) with an energy cut-off of 500 eV for each system. For the exchange correlation function, the generalized gradient approximation (GGA) method was employed. In addition, structure optimization using energy and force minimization procedures was performed. It is necessary to impose periodic boundaries in our density functional theory based calculations. Therefore, a vacuum distance was applied to avoid artificial surface interaction with neighboring unit cells along the *c*-direction. Here, the vacuum distance was assumed to be 15 Å. We have employed $14 \times 7 \times 4$ Monkhorst–Pack k-mesh for bulk and $15 \times 15 \times 1$ scheme for the cleaved systems, except for the $BiVO_4$ (004) system. For the $BiVO_4$ (004) configuration, we employed a $15 \times 9 \times 1$ Monkhorst–Pack k-mesh.

Time Resolved Photoluminescence Measurement: An inverted-type scanning confocal microscope (Picoquant Micro- Time-200, KBSI, Daegu center) was employed to obtain the time-resolved photoluminescence (TRPL) of the $BiVO_4$ photoanodes. A 375 nm single-mode pulsed diode laser with a pulse width of 240 ps and a 10 MHz repetition rate was employed as the excitation source, and an average power of < 1 μW was used. The emissions from the $BiVO_4$ photoanodes were collected with a dichroic mirror (AHF Z375RDC), a long-pass filter (AHF HQ405lp), a 50 μm pinhole, and a single-photon avalanche diode (SPAD) after passing the neutral density filter, in which the photon counting rate was maintained at approximately 1% of the excitation rate. The data acquisition was based on a time correlated single photon counting technique. The measured TRPL data were presented in the SymPhoTime operating software (ver. 5.1.3). The lifetime values were averaged as "intensity weighted lifetimes" for many samples. For each sample, we estimated the average lifetime from the TRPL images by measuring five or more $BiVO_4$ photoanodes. The data were filtered in three wavelength ranges as follows: (i) 405 ± 10 nm, (ii) 550 ± 10 nm, and (iii) 600 ± 10 nm. The three emission ranges represent (i), (ii), and (iii), respectively.

Supporting Information

Supporting Information is available from the Wiley Online Library or from the author.

Acknowledgements

This work was financially supported by the Korea Center for Artificial Photosynthesis (KCAP) located at the Sogang University (Grant No. 2009-0093885), which was funded by the Minister of Science, ICT and Future Planning (MSIP) through the National Research Foundation of Korea and the Brain Korea 21 Plus Project 2015. Y.S.K. wishes to thank Prof. Dr. J. Hong at the Department of Physic, Pukyong National University for helpful theoretical calculations of the surface energy and Dr. M. Kim at Pohang Accelerator Laboratory (PAL) for helpful XAFS measurement in PAL 10C beamline. The experiments in the Pohang Light Source (PLS) were partially supported by MSIP and POSTECH.

Received: September 2, 2015
Revised: November 6, 2015
Published online: December 10, 2015

[1] Y. Tachibana, N. Vayssieres, J. R. Durrant, *Nat. Photonics* **2012**, *6*, 511.
[2] J. Barber, *Chem. Soc. Rev.* **2009**, *38*, 185.
[3] N. S. Lewis, D. G. Nocera, *Proc. Natl. Acad. Sci. USA* **2006**, *103*, 15729.
[4] C. Liu, N. P. Dasgupta, P. Yang, *Chem. Mater.* **2014**, *26*, 415.
[5] W. Wang, J. Chen, C. Li, W. Tian, *Nat. Commun.* **2014**, *5*, 4647.
[6] A. Fujishima, K. Honda, *Nature* **1972**, *238*, 37.
[7] J. Marshal, *Nature* **2014**, *510*, 22.
[8] M. G. Kibria, F. A. Chowdhury, S. Zhao, B. Alotaibi, M. L. Trudeau, H. Guo, Z. Mi, *Nat. Commun.* **2015**, *6*, 6797.
[9] L. Ji, M. D. McDaniel, S. Wang, A. B. Posadas, X. Li, H. Huang, J. C. Lee, A. A. Demkov, A. J. Bard, J. G. Ekerdt, E. T. Yu, *Nat. Nanotechnol.* **2015**, *10*, 84.
[10] Z. Li, W. Luo, M. Zhang, J. Feng, Z. Zou, *Energy Environ. Sci.* **2013**, *6*, 347.
[11] D. Wang, H. Jiang, X. Zong, Q. Xu, Y. Ma, G. Li, C. Li, *Chem. Eur. J.* **2011**, *17*, 1275.
[12] J. K. Cooper, S. Gul, F. M. Toma, L. Chen, P. Glans, J. Guo, J. W. Ager, J. Yano, I. D. Sharp, *Chem. Mater.* **2014**, *26*, 5363.
[13] Y. Park, K. J. McDonald, K. S. Choi, *Chem. Soc. Rev.* **2013**, *42*, 2321.
[14] Z. F. Huang, L. Pan, J. J. Zou, X. Zhang, L. Wang, *Nanoscale* **2014**, *6*, 14044.
[15] Z. Chen, H. Dinh, E. Miller, *Photoelectrochemical Water Splitting: Standards, Experimental Methods, and Protocols*, Springer, New York **2013**.
[16] J. Yang, D. Wang, H. Han, C. Li, *Acc. Chem. Res.* **2013**, *46*, 1900.
[17] M. Zhou, J. Bao, Y. Xu, J. Zhang, J. Xie, M. Guan, C. Wang, L. Wen, Y. Lei, Y. Xie, *ACS Nano.* **2014**, *8*, 7088.
[18] C. Liu, J. Tang, H. M. Chen, B. Liu, P. Yang, *Nano Lett.* **2013**, *13*, 2989.
[19] P. M. Rao, L. Cai, C. Liu, I. S. Cho, C. H. Lee, J. M. Weisse, P. Yang, X. Zheng, *Nano Lett.* **2014**, *14*, 1099.
[20] T. W. Kim, K.-S. Choi, *Science* **2014**, *343*, 990.
[21] R. Li, H. Han, F. Zhang, D. Wang, C. Li, *Energy Environ. Sci.* **2014**, *7*, 1369.

[22] R. Li, F. Zhang, D. Wang, J. Yang, M. Li, J. Zhu, X. Zhou, H. Han, C. Li, *Nat. Commun.* **2013**, *4*, 1432.
[23] J. Pan, G. Liu, G. Q. Lu, H. M. Cheng, *Angew. Chem. Int. Ed.* **2011**, *50*, 2133.
[24] H. G. Yang, C. H. Sun, S. Z. Qiao, J. Zou, G. Liu, S. C. Smith, H. M. Cheng, G. Q. Lu, *Nature* **2008**, *453*, 638.
[25] S. Yang, B. X. Yang, L. Wu, Y. H. Li, P. Liu, H. Zhao, Y. Y. Yu, X. Q. Gong, H. G. Yang, *Nat. Commun.* **2014**, *5*, 5355.
[26] H. G. Yang, G. Liu, S. Z. Qiao, C. H. Sun, Y. G. Jin, S. C. Smith, J. Zou, H. M. Cheng, G. Q. (Max) Lu, *J. Am. Chem. Soc.* **2009**, *131*, 4078.
[27] F. F. Abdi, L. Han, A. H. M. Smets, M. Zeman, B. Dam, R. V. D. Krol, *Nat. Commun.* **2013**, *4*, 2195.
[28] Y. Ma, S. R. Pendiebury, A. Reynal, F. l. Formal, J. R. Durrant, *Chem. Sci.* **2014**, *5*, 2964.
[29] M. Barroso, C. A. Mesa, S. R. Pendiebury, A. J. Cowan, T. Hisatomi, K. Sivula, M. Gratzel, D. R. Klug, J. R. Durrant, *Proc. Natl. Acad. Sci. USA* **2012**, *109*, 15640.
[30] D. K. Zhong, S. Choi, D. R , Gamelin, *J. Am. Chem. Soc.* **2011**, *133*, 18370.
[31] X. Li, J. Yu, J. Low, Y. Fang, J. Xiao, X. Chen, *J. Mater. Chem. A* **2015**, *3*, 2485.
[32] W.-N. Zhao, Z.-P. Liu, *Chem. Sci.* **2014**, *5*, 2256.
[33] J. Yang, D. Wang, X. Zhuo, C. Li, *Chem. Eur. J.* **2013**, *19*, 1320.
[34] D. Kim, J. Resasco, Y. Yu, A. M. Asiri, P. Yang, *Nat. Commun.* **2014**, *5*, 4948.
[35] M. W. Kanan, J. Yano, Y. Surendranath, M. Dinca, V. K. Yachandra, D. G. Nocera, *J. Am. Chem. Soc.* **2010**, *132*, 13692.
[36] M. Newville, *Fundamentals of XAFS: Consortium for Advanced Radiation Sources*, University of Chicago, Chicago, IL **2004**.
[37] H. Dau, C. Limberg, T. Reier, M. Risch, S. Roggan, P. Strasser, *ChemCatChem* **2010**, *2*, 724.
[38] C.-S. Tan, S.-C. Hsu, W.-H. Ke, L.-J. Chen, M. H. Huang, *Nano Lett.* **2015**, *15*, 2159.
[39] C. W. Kim, S. J. Yeob, H.-M. Cheng, Y. S. Kang, *Energy Environ. Sci.* **2015**, DOI: 10.1039/C5EE02300A.